

MAE 557 Mini-Project Three

Yu Shuai

November 7, 2025

1 Choice of the pressure correction approach

The non-dimensionalized governing equations of the two-dimensional incompressible lid-driven cavity flow are given as follows:

$$\frac{\partial u_i}{\partial t} + \frac{\partial(u_j u_i)}{\partial x_j} = -\frac{\partial p}{\partial x_i} + \frac{1}{\text{Re}} \frac{\partial}{\partial x_j} \left(\frac{\partial u_i}{\partial x_j} \right), \quad (1a)$$

$$\frac{\partial u_i}{\partial x_i} = 0, \quad (1b)$$

$$u_{\perp} = 0 \quad \text{at walls}, \quad (1c)$$

$$u_{\parallel} = 0 \quad \text{at the left, right, and bottom wall}, \quad (1d)$$

$$u_{\parallel} = u_{\text{wall}} = \sin \left(\frac{2t}{\text{Re}} \right), \quad \text{at the top wall}, \quad (1e)$$

$$\frac{\partial p}{\partial \perp} = 0 \quad \text{at walls}. \quad (1f)$$

Here, we use u_{\perp} and u_{\parallel} to represent the normal and the tangential component of velocity at walls. $\frac{\partial p}{\partial \perp} = 0$ means that the derivative of pressure is 0 at walls along the wall normal directions. The relations between the dimensional variables (written in capital letters) and their dimensionless counterparts are shown as follows:

$$x_i = X_i/L, \quad (2a)$$

$$u_i = U_i/U_W, \quad (2b)$$

$$t = T/(L/U_W) = U_W T / L, \quad (2c)$$

$$p = (p - p_0)/(\rho_0 U_W^2), \quad p_0 = 1 \text{ bar}, \quad \rho_0 = p_0/(RT_0), \quad T_0 = 300 \text{ K}, \quad (2d)$$

$$U_{\text{wall}} = U_W \sin(\omega T) \implies u_{\text{wall}} = \sin \left(\frac{\omega L}{U_W} t \right) = \sin \left(\frac{\omega L^2}{2\nu} \cdot \frac{\nu}{U_W L} \cdot 2t \right) = \sin \left(\frac{2t}{\text{Re}} \right). \quad (2e)$$

and the Reynolds number is defined as $\text{Re} = U_W L / \nu$.

The pressure-correction algorithm we choose is the [Chorin's projection method](#) as shown below (here we choose the backward Euler timestepper):

$$\frac{u_i^* - u_i^n}{\Delta t} = -\frac{\partial(u_j^* u_i^*)}{\partial x_j} + \frac{1}{\text{Re}} \frac{\partial}{\partial x_j} \left(\frac{\partial u_i}{\partial x_j} \right), \quad (3a)$$

$$\frac{u_i^{n+1} - u_i^*}{\Delta t} = -\frac{\partial(p^{n+1}/\rho)}{\partial x_i}, \quad (3b)$$

$$\frac{\partial}{\partial x_j} \left(\frac{\partial(p^{n+1}/\rho)}{\partial x_j} \right) = \frac{1}{\Delta t} \frac{\partial u_j^*}{\partial x_j}. \quad (3c)$$

By utilizing this algorithm, we can ensure the solutions u_i^n satisfy the divergence-free condition. Additionally, this method is easy to implement with a first-order accuracy in time.

2 Choice of the finite volume operators

Consider a uniform collocated structured grid with $N_{x_1} \times N_{x_2}$ rectangular cells, each with size $\Delta x_1 \times \Delta x_2 = (1/N_{x_1}) \times (1/N_{x_2})$. For a single cell, we denote its center to be point P and its faces to be (e, w, c, s) . The centers of neighboring cells are then denoted as (E, W, C, S) . We now rewrite the governing equations of Chorin's method in the integral form using a second-order finite-volume-method discretization.

$$\begin{aligned}
\int_V \frac{u_i^* - u_i^n}{\Delta t} dV &= \int_V -\frac{\partial(u_j^* u_i^*)}{\partial x_j} + \frac{1}{\text{Re}} \frac{\partial}{\partial x_j} \left(\frac{\partial u_i^*}{\partial x_j} \right) dV \\
\implies \Delta x_1 \Delta x_2 \frac{(u_i^*)_P - (u_i^n)_P}{\Delta t} &= -((u_\perp^*)_e (u_i^*)_e + (u_\perp^*)_w (u_i^*)_w) \Delta x_2 - ((u_\perp^*)_n (u_i^*)_n + (u_\perp^*)_s (u_i^*)_s) \Delta x_1 \\
&\quad + \frac{1}{\text{Re}} \left(\left(\frac{\partial u_i^*}{\partial x_1} \right)_e - \left(\frac{\partial u_i^*}{\partial x_1} \right)_w \right) \Delta x_2 + \frac{1}{\text{Re}} \left(\left(\frac{\partial u_i^*}{\partial x_2} \right)_n - \left(\frac{\partial u_i^*}{\partial x_2} \right)_s \right) \Delta x_1 \\
\implies \Delta x_1 \Delta x_2 \frac{(u_1^*)_P - (u_1^n)_P}{\Delta t} &= -((u_1^*)_e^2 - (u_1^*)_w^2) \Delta x_2 - ((u_2^* u_1^*)_n - (u_2^* u_1^*)_s) \Delta x_1 \\
&\quad + \frac{1}{\text{Re}} \left(\left(\frac{\partial u_1^*}{\partial x_1} \right)_e - \left(\frac{\partial u_1^*}{\partial x_1} \right)_w \right) \Delta x_2 + \frac{1}{\text{Re}} \left(\left(\frac{\partial u_1^*}{\partial x_2} \right)_n - \left(\frac{\partial u_1^*}{\partial x_2} \right)_s \right) \Delta x_1; \\
\Delta x_1 \Delta x_2 \frac{(u_2^*)_P - (u_2^n)_P}{\Delta t} &= -((u_1^* u_2^*)_e - (u_1^* u_2^*)_w) \Delta x_2 - ((u_2^*)_n^2 - (u_2^*)_s^2) \Delta x_1 \\
&\quad + \frac{1}{\text{Re}} \left(\left(\frac{\partial u_2^*}{\partial x_1} \right)_e - \left(\frac{\partial u_2^*}{\partial x_1} \right)_w \right) \Delta x_2 + \frac{1}{\text{Re}} \left(\left(\frac{\partial u_2^*}{\partial x_2} \right)_n - \left(\frac{\partial u_2^*}{\partial x_2} \right)_s \right) \Delta x_1, \tag{4a}
\end{aligned}$$

$$\begin{aligned}
\int_V \frac{u_i^{n+1} - u_i^*}{\Delta t} dV &= \int_V -\frac{\partial(p^{n+1}/\rho)}{\partial x_i} dV \\
\implies \Delta x_1 \Delta x_2 \frac{(u_1^{n+1})_P - (u_1^*)_P}{\Delta t} &= -\frac{1}{\rho} (p_e^{n+1} - p_w^{n+1}) \Delta x_2; \\
\Delta x_1 \Delta x_2 \frac{(u_2^{n+1})_P - (u_2^*)_P}{\Delta t} &= -\frac{1}{\rho} (p_n^{n+1} - p_s^{n+1}) \Delta x_1, \tag{4b}
\end{aligned}$$

$$\begin{aligned}
\int_V \frac{\partial}{\partial x_j} \left(\frac{\partial(p^{n+1}/\rho)}{\partial x_j} \right) dV &= \frac{1}{\Delta t} \int_V \frac{\partial u_j^*}{\partial x_j} dV \\
\implies \left(\left(\frac{\partial p^{n+1}}{\partial x_1} \right)_e - \left(\frac{\partial p^{n+1}}{\partial x_1} \right)_w \right) \Delta x_2 &+ \left(\left(\frac{\partial p^{n+1}}{\partial x_2} \right)_n - \left(\frac{\partial p^{n+1}}{\partial x_2} \right)_s \right) \Delta x_1 \\
&= \frac{\rho}{\Delta t} \left(\left((u_1^*)_e - (u_1^*)_w \right) \Delta x_2 + \left((u_2^*)_n - (u_2^*)_s \right) \Delta x_1 \right). \tag{4c}
\end{aligned}$$

To obtain a second-order spatial accuracy, we evaluate quantities on cell surfaces using centered differencing and linear interpolation:

$$(u_1^*)_e = \frac{(u_1^*)_P + (u_1^*)_E}{2} \quad (\text{similar idea for other variables at other surfaces}), \tag{5a}$$

$$\left(\frac{\partial u_1^*}{\partial x_1} \right)_e = \frac{(u_1^*)_E - (u_1^*)_P}{\Delta x_1} \quad (\text{similar idea for other velocity gradients at other surfaces}), \tag{5b}$$

$$\begin{aligned}
\left(\frac{\partial p^{n+1}}{\partial x_1} \right)_e &= \frac{1}{2} \left(\frac{\partial p^{n+1}}{\partial x_1} \right)_P + \frac{1}{2} \left(\frac{\partial p^{n+1}}{\partial x_1} \right)_E \\
&= \frac{1}{2} \frac{p_E^{n+1} - p_W^{n+1}}{2\Delta x_1} + \frac{1}{2} \frac{p_{EE}^{n+1} - p_P^{n+1}}{2\Delta x_1} \quad (\text{similar idea for the pressure gradients at other surfaces}). \tag{5c}
\end{aligned}$$

where we adopt two different approaches to compute the gradients of velocity and pressure on cell surfaces, respectively.

Next, we implement the Dirichlet boundary conditions for velocity components and the Neumann boundary condition for the pressure via setting up ghost cells surrounding our computational domain. At the cell next to the wall, we have $(u_1^*)_e = ((u_1^*)_P + (u_1^*)_E)/2 = 0$, so according to (5a) we should set the value of $(u_1^*)_E = -(u_1^*)_P$. Additionally, we have $(\partial p^{n+1}/\partial x_1)_e = p_E^{n+1} - p_W^{n+1} + p_{EE}^{n+1} - p_P^{n+1} = 0$, and here we assign a symmetric configuration $p_{EE}^{n+1} = p_W^{n+1}$ and $p_E^{n+1} = p_P^{n+1}$ for simplicity and robustness.

Finally, we evaluate the divergence of velocity field using the following formula:

$$\begin{aligned}
\int_V \frac{\partial u_j^{n+1}}{\partial x_j} dV &= 0 \\
\implies ((u_1)_e^{n+1} - (u_1)_w^{n+1}) \Delta x_2 &+ ((u_2)_n^{n+1} - (u_2)_s^{n+1}) \Delta x_1 = 0 \\
\implies \frac{(u_1)_E^{n+1} - (u_1)_W^{n+1}}{2\Delta x_1} &+ \frac{(u_2)_N^{n+1} - (u_2)_S^{n+1}}{2\Delta x_2} = 0. \tag{6}
\end{aligned}$$

With the chosen pressure discretization scheme, we can ensure that the discretized Laplacian operator in the pressure Poisson equation equals to the discretized divergence of the discretized gradient, thereby enforcing the divergence-free condition rigorously everywhere in our computational domain. The only issue is that with a 9-point broad stencil for our Laplacian operator, the pressure field will potentially exhibit the so-called “Checkerboard pattern”. Nevertheless, this pattern is not guaranteed to emerge, so we just choose to be blind over this issue rather than introducing additional methods to address this problem, e.g. the Rhie-Chow interpolation.

3 Choice of the temporal schemes and solution methods

As we have mentioned in Sec. 1 and 2, the temporal scheme we have chosen for this problem is the backward Euler scheme with a first-order accuracy in time. In order to implicitly evolve the variables in time, we develop our nonlinear equation solver based on the Newton’s method. Each iteration of this Newton’s method requires the computation of the Jacobian matrix derived from eq. (4a) and the subsequent solution of the large, sparse linear system it defines.

To solve this linear system efficiently, we employ a Biconjugate Gradient (BiCG) method as the iterative solver, which is packaged in the linear algebra library *Eigen*. To accelerate the convergence of the BiCG solver, we apply an Incomplete LU factorization with Threshold (ILUT) as a preconditioner. This preconditioning strategy provides a robust and efficient balance between reducing the number of iterations and the cost of applying the preconditioner. Please see the code for further details.

Finally, we note that the discretized pressure Poisson equation eq. (4c), which can be represented in the form of $\mathbf{L}\mathbf{p} = \mathbf{b}$, has non-unique solutions as any two of them differ from each other by an arbitrary constant vector. In other words, the matrix \mathbf{L} is non-invertible. Additionally, based on our 9-point stencil (5c) and the configuration of pressure boundary condition, we know that the kernel space of \mathbf{L} should be spanned by only a single constant vector, i.e., $\text{rank}(\mathbf{L}) = N-1 < N$.

To address this non-uniqueness issue, here we enforce that the pressure field has zero mean value, i.e., $\mathbf{1}_{N^2}^\top \mathbf{p} = 0$. This can be accomplished by re-considering the solution procedure of PPE as finding a unique minimum of the following quadratic Lagrangian with a regularization term:

$$\mathcal{L}(\mathbf{p}, \lambda) = \frac{1}{2} \mathbf{p}^\top \mathbf{L} \mathbf{p} - \mathbf{p}^\top \mathbf{b} + \lambda (\mathbf{1}^\top \mathbf{p}). \quad (7)$$

At the minimum, the derivatives of \mathcal{L} with respect to \mathbf{p} and λ should both be 0, from which we have

$$\frac{\partial \mathcal{L}}{\partial \mathbf{p}} = \mathbf{L} \mathbf{p} - \mathbf{b} + \lambda \mathbf{1} = 0, \quad (8a)$$

$$\frac{\partial \mathcal{L}}{\partial \lambda} = \mathbf{1}^\top \mathbf{p} = 0. \quad (8b)$$

These two conditions can be combined into an augmented set of linear equations

$$\begin{bmatrix} \mathbf{L} & \mathbf{1} \\ \mathbf{1}^\top & 0 \end{bmatrix} \begin{bmatrix} \mathbf{p} \\ \lambda \end{bmatrix} = \begin{bmatrix} \mathbf{b} \\ 0 \end{bmatrix}, \quad (9)$$

from which we can obtain the unique solution of (\mathbf{p}, λ) . The solvability of (9) is guaranteed by the fact that the “augmented” Laplacian operator in eq. (9) is now an invertible matrix, which can be proved via demonstrating that the only solution to eq. (9) with a homogeneous right-hand side $\mathbf{b} = \mathbf{0}$ is $(\mathbf{p}, \lambda) = (\mathbf{0}, 0)$. More importantly, it can be shown that $\lambda = 0$ at the minimum of \mathcal{L} in our problem: Since the elements in the right-hand side vector \mathbf{b} are proportional to the local divergence of the tentative velocity field u_i^* , we have $\mathbf{1}^\top \mathbf{b} = 0$ according to the consistency condition of the zero-gradient pressure boundary condition (1f). Thus, we have

$$\begin{aligned} \mathbf{L} \mathbf{p} - \mathbf{b} + \lambda \mathbf{1} &= 0 \\ \implies \mathbf{1}^\top (\mathbf{L} \mathbf{p} - \mathbf{b} + \lambda \mathbf{1}) &= 0 \\ \implies (\mathbf{L} \mathbf{1})^\top \mathbf{p} - \mathbf{1}^\top \mathbf{b} + \lambda \mathbf{1}^\top \mathbf{1} &= 0 \\ \implies \mathbf{0}^\top \mathbf{p} - 0 + \lambda \mathbf{1}^\top \mathbf{1} &= 0 \\ \implies \lambda &= 0, \end{aligned} \quad (10)$$

where we utilize the property of discretized Laplacian operator \mathbf{L} that it is a symmetric matrix and that the summation of its elements along each row is 0. Consequently, the solution of pressure field \mathbf{p} given by (8) still satisfies the original PPE $\mathbf{L}\mathbf{p} = \mathbf{b}$ but now with zero mean value.

4 Approximate CFL limits

Since we are using a full-implicit timestepper, the approximate CFL limit should be infinite.

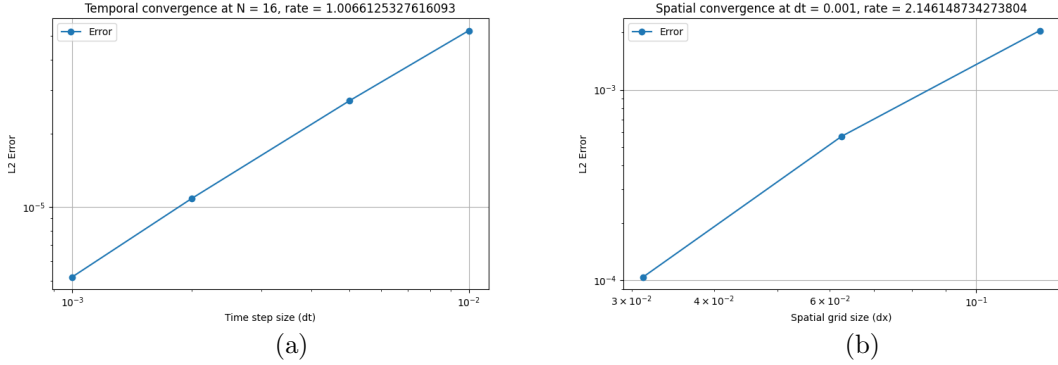


Figure 1: Temporal and spatial rate of convergence for the backward-Euler-central-differencing solver for the 2D incompressible cavity flow.

5 Algorithm in Pseudo code

See Algorithm 1 on the next page for details.

Algorithm 1 2D incompressible lid-driven cavity-flow solver based on FVM and Chorin's projection method

- 1: **Input:** dimensionless constants Re ; number of grid points: N_{x_1}, N_{x_2} with grid spacing $\Delta x_1^* = 1/N_{x_1}$, $\Delta x_2^* = 1/N_{x_2}$; timestep Δt^* ; number of timesteps N_t ; error threshold of Newton's method ε ; the upper limit of iteration times for Newton's method N_I .
 - 2: **Initialize the variables:** Set $u_1(t=0) = 0 = u_2(t=0) = 0$. Denote $\mathbf{U} = (u_1, u_2)$ as the state variable and set $\mathbf{U}^{(0)} = (u_1(t=0), u_2(t=0))$ as the initial condition.
 - 3: **Construct the “augmented” Laplacian matrix** for the pressure Poisson equation based on the 9-point stencil (4c), (5c), (9) and boundary conditions.
 - 4: **for** $j = 0$ to N_t **do** (the backward Euler scheme)
 - 5: $t^* \leftarrow j\Delta t^*$.
 - 6: Initialize the guess of the tentative variable $(\mathbf{U}^*)^{(0)} = \mathbf{U}^j$.
 - 7: Evaluate the residual $\mathbf{f}(\mathbf{U}^*)$ of the momentum equation at $\mathbf{U}^* = (\mathbf{U}^*)^{(0)}$ based on (4a), (4b), (5a), and (5b) with no-slip no-penetration boundary conditions.
 - 8: $n \leftarrow 0$.
 - 9: **while** $n \leq N_I$ and $\|\mathbf{f}((\mathbf{U}^*)^{(n)})\| \geq \varepsilon$ **do**
 - 10: Compute the Jacobian matrix $\mathbf{J}^{(n)} = (\partial \mathbf{f} / \partial \mathbf{U}^*)$ at $\mathbf{U}^* = (\mathbf{U}^*)^{(n)}$.
 - 11: Determine the update in \mathbf{U}^* : $(\mathbf{U}^*)^{(n+1)} - (\mathbf{U}^*)^{(n)} = -[\mathbf{J}^{-1} \mathbf{f}]((\mathbf{U}^*)^{(n)})$.
 - 12: $n \leftarrow n + 1$.
 - 13: **end while**
 - 14: Evaluate the divergence of the tentative velocity field $(\mathbf{U}^*)^{(n+1)}$ according to the right-hand side of (4c).
 - 15: Solve the pressure Poisson equation (4c) with augmented Laplacian matrix shown in (9) to get the zero-mean pressure field p .
 - 16: Update the velocity field to obtain the divergence-free velocity field $\mathbf{U}^{(n+1)}$ at the next timestep based on (4b).
 - 17: **end for**
-

6 Implementation and Analysis of Convergence

We study the temporal convergence via fixing $N_x = N_y = 16$ and setting $\Delta t = 10^{-2}, 5 \times 10^{-3}, 2 \times 10^{-3}, 10^{-3}$. The error is evaluated as the root-mean-square of difference between the numerical solutions and a high-fidelity solution $\tilde{\mathbf{U}}$ solved with $\Delta t = 10^{-4}$ on each grid point at the final time $t_f = 1$:

$$\epsilon = \sqrt{\frac{1}{N_{x_1} N_{x_2}} \sum_{i=0}^{N_{x_1}-1} \sum_{j=0}^{N_{x_2}-1} |\mathbf{U}((x_1)_i, (x_2)_j, t_f) - \tilde{\mathbf{U}}((x_1)_i, (x_2)_j, t_f)|_2^2}. \quad (11)$$

Fig. 1(a) shows the rate of convergence for our backward-Euler temporal discretization, which is consistent with the first-order temporal accuracy of the scheme.

Similarly, we study the spatial convergence via fixing $\Delta t = 10^{-3}$ and choose $N_x = N_y = 4, 8, 16$ and 32, respectively. The error is then evaluated as the difference between the numerical solutions and a high-fidelity solution $\tilde{\mathbf{U}}$ solved with

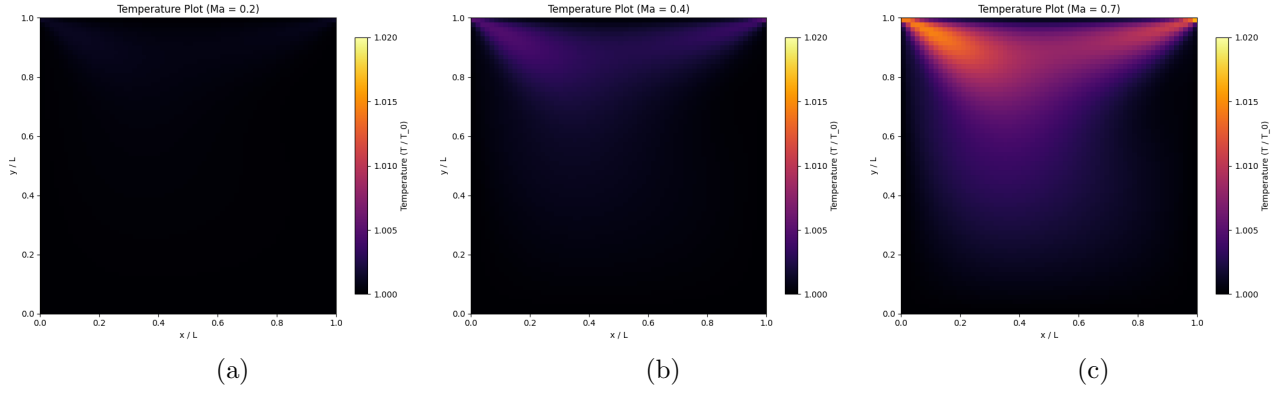


Figure 2: The temperature field at $\omega t = 10$ with $\text{Ma} = 0.2, 0.4$ and 0.7 .

$N_x = N_y = 64$ on the fixed location $(x_1, x_2) = (3/4, 3/4)$ at $t_f = 1.0$:

$$\epsilon = |\mathbf{U}(3/4, 3/4, t_f) - \tilde{\mathbf{U}}(3/4, 3/4, t_f)|_2^2. \quad (12)$$

Fig. 1(b) shows the rate of convergence for our central spatial discretization, which is consistent with the second-order accuracy of the scheme.

7 Comparison of solutions from incompressible and compressible flow solver

In this section, we compare our solution to the incompressible lid-driven cavity flow with its counterpart — the compressible lid-driven cavity flow. The compressible solutions are obtained from the exemplar code posted on Canvas. To display the trend of increasing discrepancy between these two types of solutions, we increase the Mach number Ma ranging from $0.05, 0.1, 0.2, 0.4$ to 0.7 and compare their physical fields. All solutions are solved on a 64×64 grid. The incompressible solution has a timestep $\Delta_t = 0.001$, while the compressible solutions have their respective timesteps varying with the Mach number. These computational parameters have been verified to ensure grid-converged and time-converged solutions.

We first examine the effect of the Mach number on the temperature fields. Figure 2 compares the dimensionless temperature fields at $\omega t = 10$. For the lower Mach number of $\text{Ma} = 0.2$, the dimensionless temperature is approximately 1 across the entire domain, closely approximating the isothermal conditions of the incompressible solution. However, as the Mach number increases to $\text{Ma} = 0.4$, thermal effects emerge as localized heating can be observed near the top two corners and in the center of the primary vortex. This thermal effect is further amplified at $\text{Ma} = 0.7$, where significant temperature gradients are clearly identifiable.

A similar trend is seen in the dimensionless density field displayed in Fig. 3. At $\text{Ma} = 0.4$, we begin to notice minor density variations near the top corners, where fluid compression and expansion are most intense. When the Mach number increases again to $\text{Ma} = 0.7$, these compressibility effects are far more pronounced, with a large portion of the domain experiencing significant density changes. Combining these two figures, it is suggested that the discrepancy between incompressible and compressible solutions become significant at $\text{Ma} \geq 0.4$.

We next investigate the effect of the Mach number on the kinematic field, using the streamline distribution to analyze the vortex structures, see Fig. 4. In the incompressible case, the flow exhibits a classic three-vortex structure: a large primary vortex dominating the upper half of the domain, and smaller secondary and tertiary vortices located at the bottom-left and bottom-right corners, respectively. At $\text{Ma} = 0.2$, while the temperature and density fields remained approximately uniform, the tertiary vortex already begins to break down. At $\text{Ma} = 0.4$ when thermodynamic effects of compressibility just begin to emerge, the tertiary vortex has become completely unidentifiable. Furthermore, at the even higher Mach number of $\text{Ma} = 0.7$, the enhanced dissipation associated with compressibility causes the secondary vortex to disappear as well, leaving only the primary vortex. This change in streamline field indicates that the vorticity field and velocity field are more sensitive to the change in Mach number, and both of them exhibit apparent change when Ma exceeds 0.4. This change in the streamline field may suggest that the small, fine structures in the vorticity and velocity fields are more sensitive to the Mach number than the large-scale temperature and density fields. They exhibit apparent changes (i.e., tertiary vortex breakdown) beginning as early as $\text{Ma} = 0.2$ well before the significant thermodynamic effects emerge at $\text{Ma} \geq 0.4$.

References

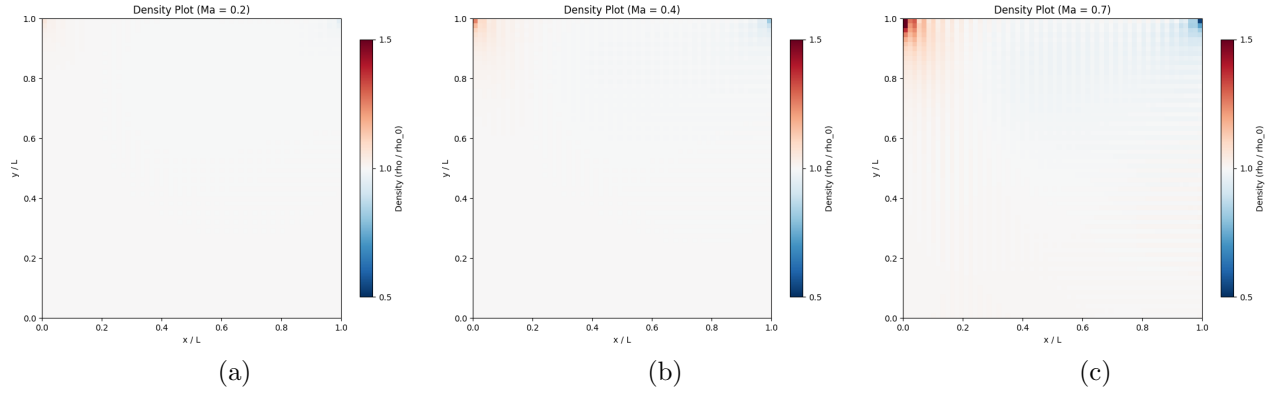


Figure 3: The density field at $\omega t = 10$ with $\text{Ma} = 0.2, 0.4$ and 0.7 .

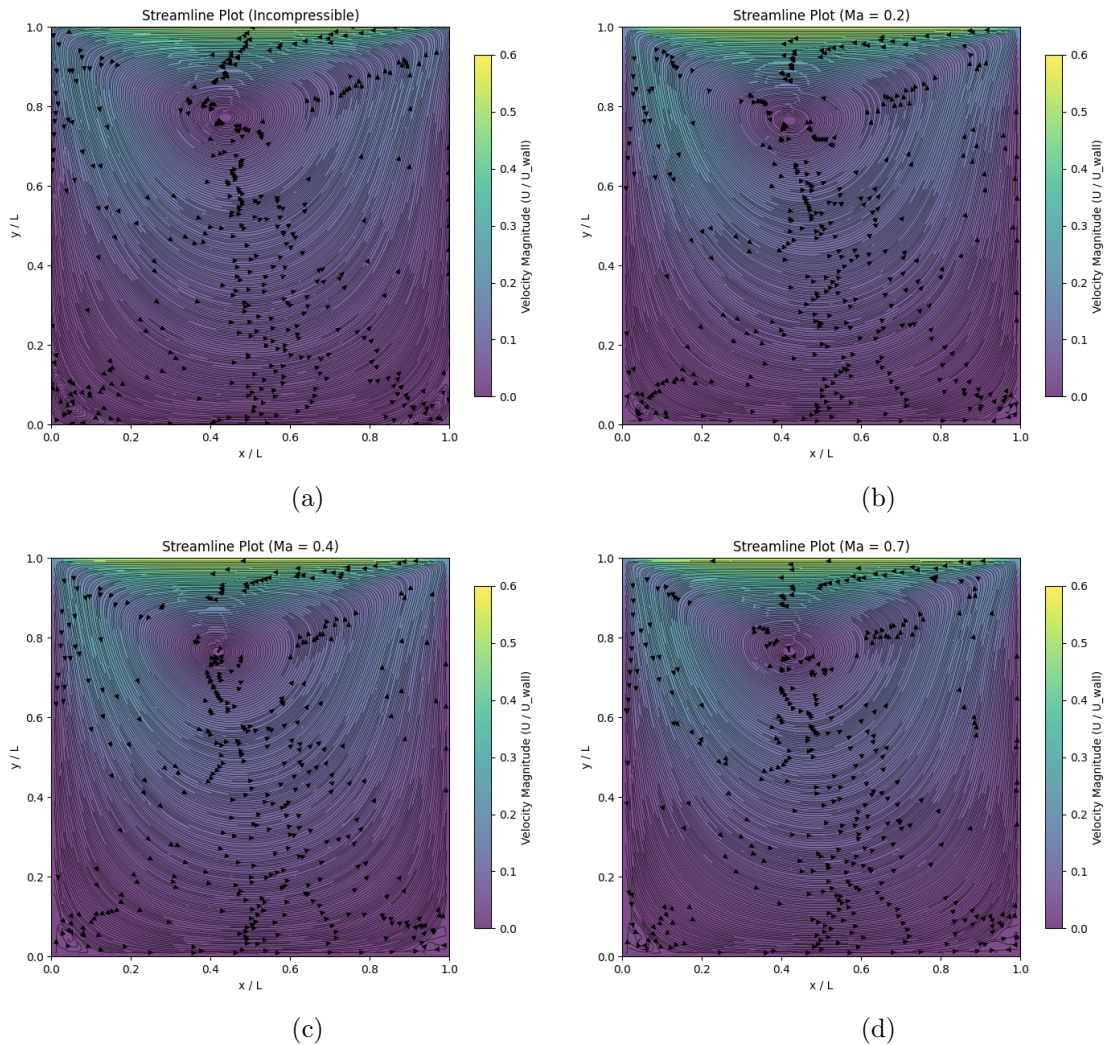


Figure 4: The distribution of streamlines at $\omega t = 10$ for the case of incompressible flow and compressible flow with $Ma = 0.2, 0.4$ and 0.7 .